Density Functional and Electrostatic Calculations of Manganese Superoxide Dismutase Active Site Complexes in Protein Environments

Jian Li,*,† Cindy L. Fisher,‡ Robert Konecny,§ Donald Bashford, and Louis Noodleman*,||

Department of Molecular Biology, TPC-15, The Scripps Research Institute, La Jolla, California 92037

Received June 25, 1998

Density functional and electrostatic methods have been applied to calculate active site geometries and the redox potential of manganese superoxide dismutase (MnSOD). The initial active site clusters were built up by including only first-shell side chain ligands and then augmented by second-shell ligands. The density functional optimized Mn−ligand bond lengths for the reduced complexes in general compared fairly well with protein crystallography data; however, large deviations for calculated Mn−OH distances were found for the oxidized active site clusters. Our calculations suggest that this deviation can be attributed to the redox heterogeneity of the oxidized protein in X-ray crystallography studies. The redox potential was calculated by treating the protein environment and the solvent bulk by a semimacroscopic electrostatic model. The protein structures were taken from the *Thermus thermophilus* enzyme. The calculated coupled redox potentials converge toward experimental values with increasing size of the active site cluster models, and the final calculated value was +0.06 V, compared to experimental values of +0.26 V determined for *Bacillus stearothermophilus* and +0.31 V in *Escherichia coli* enzymes. Using an energy decomposition scheme, the effects of the second-shell ligands and the protein and reaction fields have been analyzed.

I. Introduction

Superoxide dismutase (SOD) catalyzes the dismutation of superoxide anion radicals to hydrogen peroxide and molecular oxygen and thus protects living cells from toxic oxygen metabolites.[1−3] It has been found that SOD inhibits the peroxidation of fatty acids in inflammation and hemostasis and is anti-inflammatory in animal models. Recent evidence suggests that SOD is also involved in antiaging and anticancer processes. There are three naturally occurring forms of SOD, classified according to the redox-active metal involved: Mn, Fe, and Cu/Zn SOD. MnSODs are found in many bacteria and in the mitochondria of all eukaryotic cells, FeSODs in prokaryotes and plants, Cu/ZnSODs in eukaryotes. All of these SODs are very efficient enzymes with a rapid reaction rate, often approaching the diffusion limit for catalysis. A general "Ping-Pong" mechanism has been proposed to rationalize the reaction process in which the first $O_2^{-\bullet}$ binds to the oxidative metal center (Mn(III), Fe(III), or Cu(II) of the enzyme), transfers an electron, and releases a molecule of O_2. The second $O_2^{-\bullet}$ attaches to the reduced metal center (Mn(II), Fe(II), or Cu(I)), and an electron transfers from the metal center, which is coupled to proton transfer, forming HO_2^-.[4,5] The actual reaction pathway, however, is more complicated. For example, an inactive form of MnSOD has been observed, which results from oxidative addition of $O_2^{-\bullet}$ to a Mn(II) center and which slowly interconverts back to the active form.[6]

MnSOD is one of the best characterized of these enzymes. Several X-ray crystal structures have been reported, including human mitochondrial hMnSOD at 2.2 Å[7] and 3.0 Å[8] resolution and bacterial MnSODs from *Bacillus stearothermophilus* at 2.4 Å,[9] from *Thermus thermophilus* at 1.8 Å (oxidized) and 2.3 Å (reduced),[10] and from *Escherichia coli* at 2.1 Å resolution.[11] All of these X-ray crystallographic data reveal a similar active site structure in which the manganese is ligated by three histidines, one aspartate, and a water molecule (or hydroxyl group) in a trigonal bipyramidal arrangement. Several mutants, such as Y34F hMnSOD[12] and Q143N hMnSOD,[13] have been made and characterized. An azide derivative, which is believed to possess a binding pattern analogous to that of superoxide, has been obtained, and the X-ray crystal structural data shows that the azide binds to the metal center without loss of protein ligands.[14] Kinetic measurements by stopped-flow, pulse radi-

† E-mail: lijian@scripps.edu.
‡ Current address: Structural Bioinformatics, Inc., 10929 Technology Pl., San Diego, CA 92127.
§ Current address: Department of Chemistry, Baker Laboratory, Cornell University, Ithaca, NY 14853-1301.
|| Fax: (619) 784-8896. E-mail: lou@scripps.edu.

(1) Fridovich, I. In *Frontiers of Reactive Oxygen Species in Biology and Medicine*; Asada, K., Yoshikawa, T., Eds.; Elsevier: Amsterdam, 1994.
(2) Fridovich, I. *Annu. Rev. Biochem.* **1995**, *64*, 97.
(3) Miller, A.-F.; Sorkin, D. L. *Comments Mol. Cell. Biophys.* **1997**, *9*, 1.
(4) Tainer, J. A.; Roberts, V. A.; Fisher, C. L.; Hallewell, R. A.; Getzoff, E. D. In *A Study of Enzymes, Vol. II, Mechanism of Enzyme Action*; Kuby, S. A., Ed.; CRC Press: Boca Raton, FL, 1991.
(5) Sawyer, D. T.; Valentine, J. S. *Acc. Chem. Res.* **1981**, *14*, 393.
(6) Bull, C.; Niederhoffer, E. C.; Yoshida, T.; Fee, J. A. *J. Am. Chem. Soc.* **1991**, *113*, 4069.
(7) Borgstahl, G. E. O.; Parge, H. E.; Hickey, M. J.; Beyer, W. F.; Hallewell, R. A.; Tainer, G. A. *Cell* **1992**, *71*, 107.
(8) Wager, U. G.; Pattridge, K. A.; Ludwig, M. L.; Stallings, W. C.; Weber, M. M.; Oefner, C.; Frolow, F.; Sussman, J. L. *Protein Sci.* **1993**, *2*, 814.
(9) Parker, M. W.; Blake, C. C. F. *J. Mol. Biol.* **1988**, *199*, 649.
(10) Ludwig, M. L.; Metzger, A. L.; Pattridge, K. A.; Stallings, W. C. *J. Mol. Biol.* **1991**, *219*, 335.
(11) Edwards, R. A.; Baker, H. M.; Whittaker, M. M.; Whittaker, J. W.; Jameson, G. B.; Baker, E. N. *J. Biol. Inorg. Chem.* **1998**, *3*, 161.
(12) Guan, Y.; Hickey, M. J.; Borgstahl, G. E. O.; Hallewell, R. A.; Lepock, J. R.; O'Connor, D.; Hsieh, Y.; Nick, H. S.; Silverman, D. N.; Tainer, J. A. *Biochemistry* **1998**, *37*, 4722.
(13) Hsieh, Y.; Guan, Y.; Tu, C.; Bratt, P. J.; Angerhofer, A.; Lepock, J. R.; Hickey, M. J.; Tainer, J. A.; Nick, H. S.; Silverman, D. N. *Biochemistry* **1998**, *37*, 4731.

10.1021/ic980731o CCC: $18.00
Published on Web 02/12/1999

olysis, and spectrophotometrical techniques have been employed to characterize the inactive form of MnSOD with superoxide, and a Mn(III) side-on peroxo complex has been suggested.[6,15]

In a previous computational study, using a combined density functional and electrostatic method, we calculated the redox potential, the pK_a value of the bound water, and the electronic structure of a MnSOD active site model in aqueous solution.[16a] The calculated "absolute" redox potential for the water form was 0.17 V, compared with 0.31 V found experimentally for the *E. coli* protein. However, when the coupled protonation of $Mn^{III}OH \rightarrow Mn^{II}H_2O$ forms was included, the final coupled redox potential in a single fixed geometry was unsatisfactory (−1.09 V). The calculated pK_a value of oxidized Mn^{III}SOD showed a strong acidity as expected. The electronic structure analysis revealed that, upon reduction, the added electron was delocalized throughout all the ligands due to strong metal−ligand covalency. Recently, Whittaker et al. used the density functional method to calculate the electronic structure of a MnSOD active site metal complex.[16b] The calculated energy levels were used to calibrate the Mn(III) ligand-to-metal charge transfer (LMCT) character in the single crystal polarized spectroscopic measurement of *E. coli* MnSOD.

The current work represents our continuing effort to understand the structures, energetics, and reaction mechanisms of SOD enzymes. The coupled redox potential is recalculated with improved methods and greatly improved results. The geometries of several MnSOD active site models are optimized by density functional methods for both reduced and oxidized states in water- and hydroxyl-bound forms. These optimized geometries eliminate errors that arise from the limited resolution of X-ray data fitting and the partial reduction of oxidized samples. By using our recently developed three-region continuum dielectric method and a partial charge model for the protein atoms, the entire protein and solvent environment are used in energy calculations for the active site model.[17a] The protein structure is based on the 1.8 Å resolution structure of *T. thermophilus* MnSOD.[10] We have analyzed the results of our calculations to assess the importance of the protein and reaction field effects on the active site and on the redox process. To investigate the effects of including the second-shell ligands in the quantum active site calculations, four active site cluster models are used, with successively increasing size and complexity of the cluster models to include more of the intershell hydrogen bonds. Such calculations enable us to assess the importance of the hydrogen bonding between the active site clusters and the protein surroundings.

II. Protein Structure and Active Site Cluster Models

The structures of MnSOD from prokaryotic and eukaryotic enzymes are highly homologous. Our calculations were based on the structures of *T. thermophilus* MnSOD at 1.8 Å resolution for the "oxidized" form[10] (Brookhaven National Laboratory Protein Data Bank Code: 3MDS) and at 2.3 Å resolution for the reduced Mn(II) enzyme (M. L. Ludwig, private communication). The whole protein is a tetramer, comprising two subunits related by a dyad axis. Each subunit consists of two chains (chains A and B) of 203 residues, and the monomer chain forms two domains. The two Mn atoms, one each in chains A and B, are about 18 Å apart. We used one dimer subunit in our calculation. The structure of the dimer subunit is shown in Figure 1. The hydrogen atoms of the protein were added assuming a pH of 7, and the positions were optimized using InsightII (Discover module, Biosym/MSI) with all heavy atoms fixed.

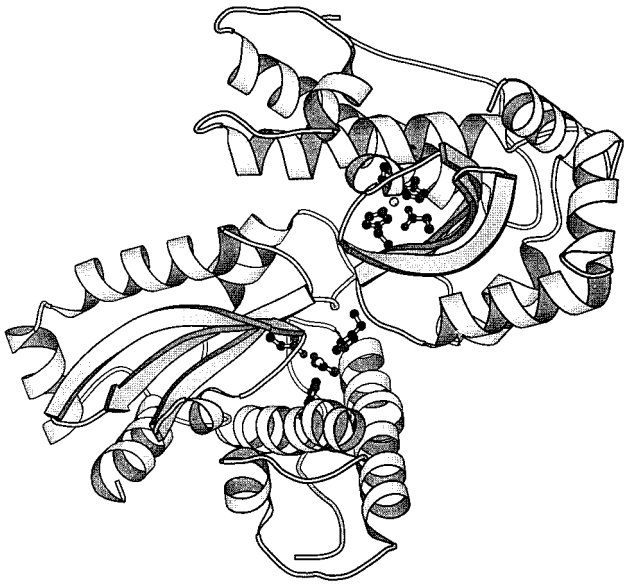

Figure 1. Protein structure (dimer subunit) of *T. thermophilus* MnSOD from protein X-ray structure data. This figure and Figure 3 were prepared using MOLSCRIPT: Kraulis, P. J. *J. Appl. Crystallogr*. **1991**, *24*, 946.

In the active site of the enzyme, the four protein side chain ligands to the Mn ion are His28, His83, Asp166, and His170. A solvent water molecule, or a hydroxyl group deprotonated from the ligated water, occupies the fifth ligand position. Our first active site model, therefore, keeps the water (hydroxyl group), three neutral imidazole rings to represent three histidine side chains, and an acetate ion representing the aspartate side chain. The CB atoms in His28, His83, and His170 and CA in Asp166 were replaced by H atoms to saturate the clusters. These atoms lie at the junction between the quantum region and the classical region, and a special treatment was used in the calculations. This active site model is the same as in our previous work[16] and is designated as model A. In some cases, we also denote model A as $MnL_4(H_2O)$ or $MnL_4(OH)$, to specify whether the fifth ligand is H_2O or OH^-. Overall, the active site is a charged cluster, which can form strong hydrogen bonds to the protein side chain or backbone atoms surrounding the active site cluster. To account for such effects, the active site quantum model was expanded to include an acetate anion, which corresponds to Glu169B H-bonds to the hydrogen atom, HD1, in the imidazole ring of His170. The ND1···OE2 distance is about 2.82 Å, and the hydrogen bond is strengthened by the charged groups (we note also that Glu169B comes from the chain B subunit). This model is denoted as model B. We further augmented the active site model by adding two simple amine molecules, forming two hydrogen bonds to the oxygens in the two acetates, which correspond to the carboxylate-backbone hydrogen bond, OD2(Asp166)···H···N(Trp168) and OE1-(Glu169B)···H···N(His170). The O−N distances are 3.12 and 3.65 Å, respectively, in the oxidized cluster. This model is denoted as model C. The biggest cluster model, model D,

(14) Lah, M. S.; Dixon, M. M.; Pattridge, K. A.; Stallings, W. C.; Fee, J. A.; Ludwig, M. L. *Biochemistry* **1995**, *34*, 1646.
(15) Hus, J. L.; Hsieh, Y.; Yu, C. K.; O'Connor, D.; Nick, H. S.; Silverman, D. N. *J. Biol. Chem.* **1996**, *271*, 17687.
(16) (a) Fisher, C. L.; Chen, J. L.; Li, J.; Bashford, D.; Noodleman, L. *J. Phys. Chem.* **1996**, *100*, 13498. (b) Whittaker, M. M.; Ekberg, C. A.; Edwards, R. A.; Baker, E. N.; Jameson, G. B.; Whittaker, J. W. *J. Phys. Chem. B* **1998**, *102*, 4668.
(17) (a) Li, J.; Nelson, M. R.; Peng, C. Y.; Bashford, D.; Noodleman, L. *J. Phys. Chem. A* **1998**, *102*, 6311. (b) Chen, J. L.; Noodleman, L.; Case, D. A.; Bashford, D. *J. Phys. Chem.* **1994**, *98*, 10059.

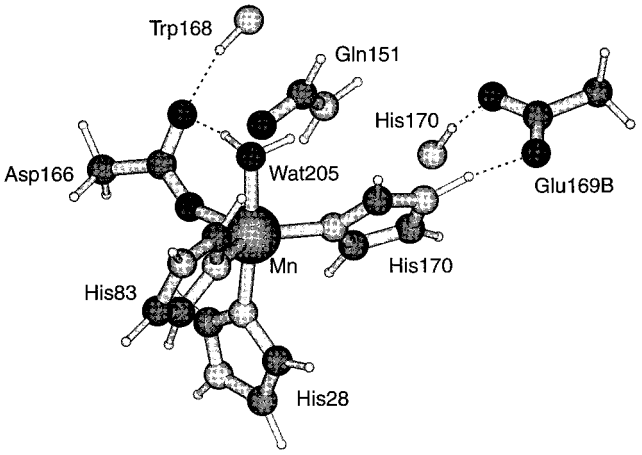

Figure 2. MnSOD active site cluster model D.

Table 1. Active Site Cluster Models

cluster model	residue side chain ligand
A	$MnL_4(H_2O/OH^-)$ (L_4 = His28, His83, Asp166, His170)
B	$MnL_4(H_2O/OH^-)$ + Glu169B
C	$MnL_4(H_2O/OH^-)$ + Glu169B + $2NH_3$
D	$MnL_4(H_2O/OH^-)$ + Glu169B + $2NH_3$ + Gln151

includes a formamide to represent the Gln151 side chain, which can form a hydrogen bond to the ligated H_2O or OH^- group, and is believed to play an important role in the proton relay system of the enzyme.[12] Figure 2 depicts the active site cluster model D. Table 1 summarizes the side chain ligands used in all these four cluster models. The starting geometries of all these active site cluster models were built up from the crystal structure data, while the final geometries and the corresponding energetics were computed by density functional methods as described in the next section.

III. Computational Methodology

The computations in this paper are based on our recently developed method which incorporates both the protein environment and solvent effects in density functional calculations. The theoretical background and a detailed discussion of the method can be found elsewhere.[17] In brief, the calculation is a stepwise procedure. First, density functional (DF) calculations are carried out to optimize the geometries of the active site cluster model and to compute the gas phase energetics of the corresponding optimized structures. Second, a set of atomic point charges for the active site cluster is fitted to best represent the molecular electrostatic potential (ESP) generated by DF calculations. Third, the optimized active site cluster is docked back to the protein structure, and then the MEAD (macroscopic electrostatics with atomic detail) program is employed to calculate the protein field and solvent field energies.[17] The details of these steps and relevant parameters are discussed below.

The Amsterdam density functional package (ADF, version 2.3)[18] was employed to compute the geometries and energies of the active site clusters. The ADF basis set IV was used for Mn and basis set III for C, N, O, and H, which correspond to uncontracted triple-ζ Slater-type orbitals (STO) for the 4s, 4p, and 3d valence orbitals of Mn, double-ζ STOs for 2s and 2p valence orbitals of C, N, and O augmented with a 3d polarization orbital, and double-ζ STO for 1s of H with a 2p polarization orbital.[19] The inner core orbitals were treated by the frozen core approximation. An auxiliary charge density fit set that consists of s, p, d, f, and g STO functions accompanies the corresponding orbital basis sets IV and III and was adopted to fit the molecular density and used to calculate the Coulomb and exchange potentials.[20] The numerical integration scheme was the polyhedron method developed by te Velde et al.[21] Geometry optimization was carried out using an analytic gradient method implemented by Verluis et al.[22] The optimization used the Newton−Raphson method, and the Hessian was updated with the Broyden−Fletcher−Goldfard−Shanno scheme.[23] Convergence criteria were set to 0.005 Å in coordinates and 0.01 in the norm of all gradient vectors. For charged and spin-polarized complexes such as the present MnSOD active site cluster models, our previous calculations have shown that a special form of the local density approximation (LDA) gives rather good metal−ligand distances.[24] The geometry optimization in this paper was thus done at the LDA level, with the Vosko−Wilk−Nusair (V) parametrization[25] and with a local correction term introduced by Stoll et al. (S).[26] We designate the method as VS. The Becke (B)[27] and Perdew (P)[28] nonlocal corrections to the exchange and correlation terms, the so-called VBP method, were used in the single-point self-consistent field calculation of energies at the VS optimized active site cluster structures. To deal with the spin polarization in these active site clusters, the spin-unrestricted method was used for all density functional calculations.

The ESP atomic charges were generated by using a modified version of the CHELPG code of Breneman and Wiberg.[29] This set of point charges represents a best fit of the molecular electrostatic potential calculated by DF methods at the VBP level. The total net charge of the active site cluster and the three Cartesian dipole moment components from ADF calculations were adopted as constraint conditions for the fit. The fitted points lay on a cubic grid within the envelope between the van der Waals radius and the outer atomic radius with a grid spacing of 0.2 Å. The outer atomic radius for all atoms used was 5.0 Å, and the van der Waals radii for $Mn^{2+/3+}$, N, C, O, and H were 1.50, 1.55, 1.67, 1.40, and 1.20 Å, respectively. To minimize the uncertainties in the fitting procedure, the singular value decomposition (SVD) method[30,31] was introduced into the code

(18) ADF 2.3.0: Department of Theoretical Chemistry, Free University of Amsterdam, 1997.

(19) (a) Snijders, J. G.; Baerends, E. J.; Vernooijs, P. *At. Nucl. Data Tables* **1982**, *26*, 483. (b) Vernooijs, P.; Snijders, J. G.; Baerends, E. J. *Slater Type Basis Functions for the Whole Periodic System*; internal report; Free University of Amsterdam: Amsterdam, The Netherlands, 1981.

(20) Krijn, J.; Baerends, E. J. *Fit Functions in the HFS-method*; internal report (in Dutch); Free University of Amsterdam: Amsterdam, The Netherlands, 1984.

(21) (a) Boerrigter, P. M.; te Velde, G.; Baerends, E. J. *Int. J. Quantum Chem*. **1988**, *33*, 87. (b) te Velde, G.; Baerends, E. J. *J. Comput. Phys.* **1992**, *99*, 84.

(22) Versluis, L.; Ziegler, T. *J. Chem. Phys.* **1988**, *88*, 322.

(23) (a) Schlegel, H. B. In *Ab initio Methods in Quantum Chemistry, Vol. I;* Lawley, K. P., Ed.; *Adv. Chem. Phys.* 67; Wiley: New York, 1987. (b) Head, J. D.; Zerner, M. C. *Adv. Quantum Chem.* **1988**, *20*, 1.

(24) Li, J.; Noodleman, L. In *Spectroscopic Methods in Bioinorganic Chemistry*; ACS Symposium Series 692; Solomon, E. I., Hodgson, K. O., Eds.; American Chemical Society: Washington, DC, 1998; p 179.

(25) Vosko, S. H.; Wilk, L.; Nusair, M. *Can. J. Phys.* **1980**, *58*, 1200.

(26) (a) Stoll, H.; Pavlidou, C. M. E.; Preuss, H. *Theor. Chim. Acta* **1978**, *49*, 143. (b) Stoll, H.; Golka, E.; Preuss, H. *Theor. Chim. Acta* **1980**, *55*, 29.

(27) Becke, A. D. *J. Chem. Phys*. **1986**, *84*, 4524.

(28) Perdew, J. P. *Phys. Rev. B* **1986**, *33*, 8822. Erratum: Perdew, J. P. *Phys. Rev. B* **1986**, *34*, 7406.

(29) Breneman, C. M.; Wiberg, K. B. *J. Comput. Chem.* **1990**, *11*, 361.

(30) Press, W. H.; Flanery, B. P.; Teukolsky, S. A.; Vetterling, W. T. *Numerical Recipes, The Art of Scientific Computing*; Cambridge University Press: Cambridge, 1986.

to obtain a model with stable atomic charges and an accurate molecular dipole moment. To keep charge conservation and to avoid unphysical charge interactions, all junction H atoms were excluded from the charge fitting procedure by setting the atomic charges of these H atoms to 0, but they were included in the construction of the fitting grid envelope. For the atoms in the protein (except those in the active site cluster), the widely used PARSE charges and radii were assigned to all atoms.[32]

Once the charges of the active site cluster and protein atoms have been assigned, the active site cluster with optimized geometry needs to be docked back into the protein in order to compute the electrostatic interaction between the cluster, protein, and solvent. The docking process was implemented with the Xfit program developed by McRee et al.[33] Using this method, the optimized active site cluster was superimposed on the original active site cluster extracted from the X-ray structure with a least-squares fitting scheme. The typical root-mean-square (rms) errors of such a docking procedure are usually smaller than 0.3 Å for all atoms in the whole cluster.

The MEAD (macroscopic electrostatics with atomic detail) program[34] was employed to calculate the protein field energy and reaction field energy, E_{pr}. The protein field interaction energy E_p is obtained from the electrostatic potential of all the protein charges (screened by the protein and solvent dielectric media) acting on the partial atom charges of the active site quantum cluster. By contrast, the reaction field energy E_r is generated by the active site cluster charges which polarize the protein and solvent dielectrics. This polarization potential acts back on the active site cluster charges. Detailed mathematical analyses of the reaction field and protein field energy terms can be found elsewhere.[17,31,34] The MEAD program solves the Poisson or linearized Poisson−Boltzmann equation by a numerical finite-difference method in three regions, and the dielectric constants are 1, 4, and 80 for active site, protein, and solvent regions, respectively. The dielectric constant 4, adopted for the protein region, allows some mobility of the protein dipoles and accounts for some reorientational relaxation of the protein in an approximate way.[35] For the purpose of defining the dielectric boundary, atomic radii of 1.50 ($Mn^{2+/3+}$), 1.55 (N), 1.67 (C), 1.40 (O), and 1.20 (H) Å were chosen. These N, C, O, and H radii are very similar to the PARSE radii, suggested by Sitkoff, Sharp, and Honig[32] and widely used for protein electrostatics. The "solute interior" was defined as the region inaccessible to any part of a probe sphere of radius 1.4 Å rolling on the molecular surface of the atomic spheres. The boundary between the interior and exterior so defined is equivalent to Connolly's definition of the molecular surface.[36] The resulting Poisson equation was solved by using an over-relaxation algorithm on successively finer grids of size 61^3, 81^3, and 101^3 with linear spacings of 1.0, 0.25, and 0.15 Å, respectively. In the present paper, the one-step approach rather than the iterative self-consistent reaction field (SCRF) was used to estimate protein field and reaction field energies. Our previous work has shown that E_p and E_r obtained in this way are very similar to those from the full SCRF calculations.[17] For comparison, the solvation energy of the active site cluster in a pure dielectric solvent was also calculated at two dielectric constants, $\epsilon = 4$ and 80, by the MEAD method.

Taking the $MnL_4(H_2O)$ active site cluster as an example, based on the calculated DF energy $E[MnL_4(H_2O)]$ and the corresponding protein and reaction field energy $E_{pr} = (E_p + E_r)$, the redox potential in going from Mn(III) to Mn(II) in MnSOD can be calculated as

$$\Delta E_{redox}°[MnL_4(H_2O)] = \{E[Mn^{3+}L_4(H_2O)] - E[Mn^{2+}L_4(H_2O)]\} + \{E_{pr}[Mn^{3+}L_4(H_2O)] - E_{pr}[Mn^{2+}L_4(H_2O)]\} + \Delta SHE = IP_{red} + \Delta E_{pr}(redox) - 4.43 \quad (1)$$

where IP_{red} is the gas phase ionization potential of the reduced cluster and ΔSHE is the standard hydrogen electrode potential, −4.43 V.[37] Similarly, the pK_a value of the water molecule bound to the Mn center for the active site model $MnL_4(H_2O)$ can be calculated from the obtained energy terms as

$$1.37\ pK_a = \{E[MnL_4(OH)] + E[H^+] - E[MnL_4(H_2O)]\} + \{E_{pr}[MnL_4(OH)] - E_{pr}[MnL_4(H_2O)]\} - 267.7 + E_{corr} = PA + \Delta E_{pr}(deproton) - 267.7 \quad (2)$$

where −267.7 kcal/mol comes from the sum of solvation free energy of a proton (−260.5 kcal/mol) plus the translation entropy contribution to the gas phase free energy of a proton ($-T\Delta S_{gas}(H^+) = -7.2$ kcal/mol at 298 K). E_{corr} is a correction term to the proton affinity PA, including zero point energy (ΔZPE) and $(5/2)RT$ work. We used the same values for this term as in our previous calculations (ΔZPE = −7.1 and −7.7 kcal/mol for Mn^{2+} and Mn^{3+} cases, respectively).[38] Equations 1 and 2 can be applied directly to other active site clusters as long as the corresponding energy terms are correctly substituted.

For MnSOD, there is a consensus that a ligated H_2O is the fifth ligand of the Mn ion in the reduced enzyme (Mn^{2+}-H_2O) while the corresponding ligand is an OH^- group in the oxidized enzyme (Mn^{3+}-OH), due to the high acidity expected for Mn^{3+}-bound water. [6] The experimentally measured redox potential then corresponds to the process

$$Mn^{3+}\text{-OH enzyme} + H^+ + e^- \rightarrow Mn^{2+}\text{-}H_2O \text{ enzyme} \quad (3)$$

and therefore, we can calculate the coupled redox potential for eq 3 at pH = 7 according to

$$\Delta E_{redox}°(coupled) = \Delta E_{redox}°[MnL_4(OH)] + 1.37\ \{pK_a[Mn^{2+}L_4(H_2O)] - 7.0\}/23.06 \quad (4)$$

The calculated $\Delta E_{redox}°$(coupled) can be compared directly with experimental values.

IV. Results and Discussion

1. Geometry Optimization of Native Active Site Clusters. The high-resolution protein X-ray crystallographic data can be used to construct the coordination geometry of a metal active site cluster. However, active site cluster models built up in this way are not accurate enough for quantum mechanical energy calculations due to the significant uncertainties in metal−ligand

(31) (a) Mouesca, J.-M.; Chen, J. L.; Noodleman, L.; Bashford, D.; Case, D. A. *J. Am. Chem. Soc.* **1994**, *116*, 11898. (b) Francl, M. M.; Carey, C.; Chirlian, L. M.; Gange, D. M. *J. Comput. Chem.* **1996**, *17*, 367.
(32) Sitkoff, D.; Sharp, K. A.; Honig, B. *J. Phys. Chem.* **1994**, *98*, 1978.
(33) McRee, D. E.; Israel, M. In *Crystallographic Computing, Vol. 7*; Bourne, E., Watenpaugh, K., Eds.; Oxford University Press: Oxford, in press.
(34) (a) Bashford, D.; Karplus, M. *Biochemistry* **1990**, *29*, 10219. (b) Lim, C.; Bashford, D.; Karplus, M. *J. Phys. Chem.* **1991**, *95*, 5610.
(35) (a) Harvey, S. C. *Protein* **1989**, *5*, 78. (b) Sharp, K.; Honig, B. *Annu. Rev. Biophys. Biophys. Chem.* **1990**, *19*, 301. (c) Simonson, T.; Brooks, C. L. *J. Am. Chem. Soc.* **1996**, *118*, 8452.
(36) Connolly, M. L. *Science* **1983**, *221*, 709.
(37) Reiss, H.; Heller, A. *J. Phys. Chem.* **1985**, *89*, 4207.
(38) Li, J.; Fisher, C. L.; Chen, J. L.; Bashford, D.; Noodleman, L. *Inorg. Chem.* **1996**, *35*, 4694.

Table 2. Comparison of Optimized and Experimental Geometries of MnSOD Active Site Clusters[a]

	H_2O form					OH^- form					exptl	
	A(full)[b]	A	B	C	D	A(full)	A	B	C	D	Ludwig[c]	Tainer[d]
reduced												
Mn−O(Wat)	2.144	2.329	2.330	2.337	2.368	1.968	1.913	1.919	1.919	2.003	2.23	
Mn−N(His170)	2.140	2.116	2.044	2.038	2.043	2.157	2.158	2.114	2.116	2.097	2.21	
Mn−N(His28)	2.182	2.141	2.183	2.173	2.169	2.297	2.250	2.299	2.297	2.149	2.14	
Mn−N(His83)	2.099	2.087	2.108	2.115	2.143	2.163	2.137	2.144	2.156	2.183	2.12	
Mn−O(Asp166)	2.022	1.942	1.970	1.982	1.968	2.036	2.030	2.068	2.111	2.110	1.84	
oxidized												
Mn−O(Wat)	1.844	1.982	2.014	2.124	2.008	1.760	1.781	1.792	1.786	1.810	2.08	2.08
Mn−N(His170)	2.022	2.010	1.963	2.001	1.968	2.039	2.025	1.990	1.969	1.973	2.17	2.07
Mn−N(His28)	1.972	1.951	1.956	2.051	1.970	2.036	2.046	2.052	2.052	2.039	2.13	2.09
Mn−N(His83)	2.033	2.026	2.041	2.083	2.048	2.052	2.047	2.051	2.060	2.073	2.11	2.07
Mn−O(Asp166)	2.024	1.858	1.891	1.920	1.867	1.950	1.889	1.915	1.922	1.915	1.77	1.93

[a] Bond lengths in angstroms. [b] A(full): full optimization. [c] From *T. thermophilus* MnSOD, ref 10. [d] From human MnSOD, ref 7.

bond lengths and angles (see also our discussion of redox heterogeneity below). We instead optimized the geometries for all active site cluster models A−D for both the Mn(II) and Mn(III) states, and for the water and hydroxyl bound forms. Since the clusters are large and the optimized clusters need to be docked back to the protein for electrostatic calculations, we only carried out a partial geometry optimization for most of the models. Only the first-layer geometries, including all Mn−N and Mn−O distances, N−Mn−N, N−Mn−O, and O−Mn−O angles, and all geometrical parameters of bound H_2O and OH^- were allowed to change. The internal geometries and the orientations of imidazoles and acetates were kept fixed during the optimization as taken from the *T. thermophilus* X-ray structures (see below). In model B, the ND1···OE2 distance (2.82 Å), the internal geometry, and the orientation of the acetate (from Glu169B) were fixed, and only ND1···H or H···OE2 distances were added to the optimization parameters in model A. Similar treatment was applied to model D to handle the formamide ligand (from Gln151), where the Mn···NE2 distance (4.64 Å for the Mn^{3+} form and 4.66 Å for the Mn^{2+} form) and the parameters of carbonyl group were fixed, while the geometries of the two H atoms linked to NE2 and the ligated H_2O or OH^- group were optimized. In models C and D, the N···OD1 distance (from Trp168 main chain−Asp166, 3.12 Å) and the N···OE1 distance (from His170 main chain−Glu169B, 3.65 Å) were fixed and optimization was done on the hydrogen atom positions in the N···H···OE1 or N···H···OD1 hydrogen bonds. For comparison, a full geometry optimization was done only for model A. The optimized metal−ligand bond lengths, together with the protein X-ray data, are summarized in Table 2.

For reduced clusters, the fifth ligand is expected to be a water molecule. Our optimized Mn−O and Mn−N distances in the four models compare fairly well with X-ray data, with an average error smaller than 0.1 Å. The best agreement can be found in the smallest model, A, where the average deviation for the five metal−ligand bond lengths is just 0.075 Å, while for the largest model D, the average deviation is 0.097 Å. (Both of these average deviations are within expected experimental bond length uncertainties given the resolution of the X-ray data.[10]) The Mn−N(His170) distance is shortened by forming the ND1(His170A)···H···OE2(Glu169B) hydrogen bond; this trend prevails both in the reduced/oxidized states and H_2O/OH^- forms.

For the oxidized cluster, two sets of X-ray data have been determined, one for *T. thermophilus* MnSOD[10] and one for human mitochondrial MnSOD.[7] We use the OH^- bound form to compare with the X-ray data. Among the five Mn−ligand bond lengths, three Mn−N distances agree well between constrained optimized structures and X-ray data, but a larger deviation (about 0.3 Å) is observed for the Mn−OH distance. This difference may be partially attributed to difficulties in accurately determining short Mn−O distances even in good resolution protein structures; however, other factors are also likely to contribute to this discrepancy. In a careful spectral study of *E. coli* MnSOD, Whittaker reported redox heterogeneity as monitored by EPR signals, which clearly indicated a physical mixture of Mn(II) and Mn(III) forms in enzymes isolated in the normal "oxidized resting" state (this was the state assumed on the basis of "oxidizing" conditions, and the observed color in the X-ray structures cited below).[39] The mixing ratio may vary between preparations, but the Mn(II) fraction can be up to approximately 50% of the total. On the basis of this observation, we have averaged the Mn−ligand distances between Mn(II)−OH_2 and Mn(III)−OH forms and the data are shown in Table 3. These averaged Mn−ligand distances, especially Mn−O(H_2O/OH^-) distances, are now in excellent agreement with X-ray data, particularly for the set from Tainer et al.[7] These results lead us to expect that the two sets of X-ray data were determined for a physical mixture of Mn(III) and Mn(II) enzymes, instead of corresponding to the pure Mn(III) enzyme, consistent with the EPR observations of Whittaker.[39] Our constrained geometry optimization results then can be applied to estimate the mixture ratio of the Mn(III) and Mn(II) forms in the enzymes. From a least-squares fit, we estimate that the Mn(III)/[Mn(II) + Mn(III)] ratios in the two sets of X-ray data from Tainer et al.[7] and Ludwig et al.[10] are 0.48 and 0.56, both very close to 0.5. Recently, Baker et al.[11] reported the protein X-ray data for *E. coli* MnSOD, and the data are included in Table 3 as well. They claimed that the observed Mn−O(H_2O/OH^-) distance corresponds to a mixture of Mn(III)−OH and Mn(II)−OH moieties.[11]

Table 3. Averaged Geometries[a]

	mixed (H_2O/OH^-) form					exptl		
	A(full)[b]	A	B	C	D	Ludwig[c]	Tainer[d]	Baker[e]
Mn−O(Wat)	1.952	2.055	2.061	2.062	2.089	2.08	2.08	2.24
Mn−N(His170)	2.090	2.071	2.017	2.004	2.008	2.17	2.07	2.19
Mn−N(His28)	2.109	2.094	2.118	2.113	2.104	2.13	2.09	2.19
Mn−N(His83)	2.076	2.067	2.080	2.088	2.108	2.11	2.07	2.25
Mn−O(Asp166)	1.986	1.916	1.943	1.952	1.942	1.77	1.93	2.05

[a] The bond lengths (Å) are calculated according to $R_{M-L} = (1/2)\{R_{M-L}[\text{reduced } MnL_5(H_2O)] + R_{M-L}[\text{oxidized } MnL_5(OH)]\}$. [b] A(full): full optimization. [c] From *T. thermophilus* MnSOD, ref 10. [d] From human MnSOD, ref 7. [e] From *E. coli* MnSOD, ref 11.

(39) Whittaker, J. W.; Whittaker, M. M. *J. Am. Chem. Soc.* **1991**, *113*, 5528.

However, according to our optimized Mn−O distances, the observed long Mn−O distance (2.24 Å) in this enzyme is closer to the Mn(II)−OH_2 distance.

In a very recent density functional calculation of active site cluster models, Whittaker et al. carried out geometry optimizations on $Mn^{III}L_4(OH)$, $Mn^{II}L_4(OH)$, and $Mn^{II}L_4(H_2O)$.[16b] For the $Mn^{III}L_4(OH)$ complex, their optimized Mn−ligand distances (Mn−OH, 1.77 Å; Mn−O(Asp), 1.94 Å; Mn−N(His), 2.10, 2.07, and 2.10 Å, respectively) are very similar to our results, especially the fully optimized one A(full) (see Table 2). This high level of agreement between the two sets of calculations is particularly significant since they were carried out completely independently, with different density functional computer programs and different exchange-correlation functionals. It is not clear if their optimization was full, although a C_s symmetry was applied by rotating the axial imidazole and the acetate ligands slightly. They noticed a large difference between the optimized Mn−OH distance (1.77 Å) and the experimental Mn−OH distance (2.18 Å) as observed in *E. coli* MnSOD,[11] and they also attributed this discrepancy to the heterogeneity in the metal oxidation state in the protein crystals, along with some other factors like in vacuo geometry optimization and imprecise crystallographic refinement.[16b] Similarly, the geometries reported by Whittaker et al. for both the $Mn^{II}L_4(OH)$ and $Mn^{II}L_4(H_2O)$ forms closely match our calculated geometries with the A(full) model and show a substantial lengthening of the Mn(II)−OH and Mn(II)−H_2O bonds compared with $Mn^{III}OH$ (Table 2).

It is of special interest to compare our calculated geometries from the constrained and full optimizations. The fully optimized structures, which correspond to a gas phase, free $MnL_4(H_2O)$ or $MnL_4(OH)$ cluster in a vacuum, are similar to those optimized with constraints. The trigonal bipyramidal geometry is retained in the full optimization and the optimized free cluster geometries can be superimposed on the clusters in the protein almost precisely, by slight shifting or tilting of imidazole rings and acetate; see Figure 3. This is a direct indication that the Mn coordination sphere is not strongly strained in the protein. A close look at the geometries from two different optimizations (models A(full) and A(constrained)) still reveals some differences. For $MnL_4(H_2O)$, the Mn−O(H_2O) distance from full optimization is obviously shorter than the one from the corresponding constrained optimization for both reduced and oxidized forms, but the Mn−O(Asp166) distance shows the opposite trend. The tilting of the acetate ligand in the free unconstrained cluster allows another O atom to be close to an H atom in the ligated H_2O, forming a strong O(Asp)···H···O(Wat) hydrogen bond. This hydrogen bond is so strong that the proton is completely transferred to acetate in free $Mn^{III}L_4(H_2O)$, and there is a related, but smaller, H-bond strengthening in $Mn^{II}L_4(H_2O)$. By contrast, in the constrained geometries (models A−D), the O(Asp)···H···O(Wat) hydrogen bond is weakened by competition with the O(Asp)···H−N(Trp) hydrogen bond. This competition has both energetic and geometric effects (see Figure 3 and Table 2). It can be concluded at this point that, although the protein does not dramatically distort the Mn coordination sphere and the electronic structure of the active site clusters, it at least modulates the hydrogen-bond network which connects the active site cluster and protein side chains and backbone. Such a modulation implies a significant effect on the properties of the enzymes, as can be seen in next section. Very recently, Vance and Miller[40] studied the redox potentials of native *E. coli* FeSOD and Fe-substituted *E. coli* MnSOD. They found a large redox potential shift (almost 0.5 V) upon putting Fe ion in different protein environments, and thus they concluded that different coordinated solvent protonation in these two proteins could account for the large difference between the redox potentials of the two enzymes.

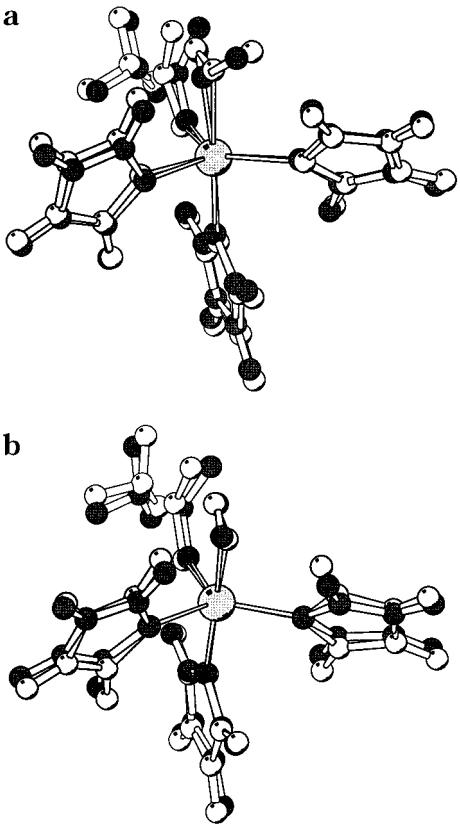

Figure 3. Superimposition of MnSOD active site cluster structures: (a) from full DF optimization and protein X-ray data, $Mn^{II}(H_2O)$ form, model A; (b) from full DF optimization and constrained optimization, $Mn^{III}(OH^-)$ form, model A. Filled symbols represent full DF optimization structures, and open symbols represent X-ray structure in part a and constrained optimization structure in part b.

Ryde et al.[41a] applied the DFT method to fully optimize the active site cluster of blue copper proteins and also found that the optimized vacuum structures of the Cu(II) model coincide well with the crystal structures. According to this result, they raised strong objections to the hypothesis of an entatic or induced-rack state in blue copper proteins. However, other spectroscopic studies and calculations supported some role for the entatic effect, with variable magnitude across the range of blue copper proteins and structures.[41b,c] These studies and comparative X-ray structural studies show differences in the first-shell ligand geometries for various blue copper centers even with all the same ligand side chains coordinated to the copper ion. This implies some entatic influence, and the relevant question is how large the energetic influences are and what the protein contributions are. Similar questions remain open for MnSOD, FeSOD, and other metalloproteins.

2. Geometry Optimization of Azide Complexes. In the MnSOD active site, the Mn cation adopts a five-coordinate, trigonal bipyramidal configuration. From the viewpoint of coordination geometry, the Mn site is unsaturated and the sixth

(40) (a) Vance, C. K.; Miller, A.-F. *J. Am. Chem. Soc.* **1998**, *120*, 461. (b) Vance, C. K.; Miller, A.-F. *Biochemistry* **1998**, *37*, 5518.

(41) (a) Ryde, U.; Olsson, M. H. M.; Pierloot, K.; Roos, B. O. *J. Mol. Biol.* **1996**, *261*, 586. (b) Guckert, J. A.; Lowery, M. D.; Solomon, E. I. *J. Am. Chem. Soc.* **1995**, *117*, 2817. (c) LaCroix, L. B.; Shadle, S. E.; Wang, Y.; Averill, B. A.; Hedman, B.; Hodgson, K. O.; Solomon, E. I. *J. Am. Chem. Soc.* **1996**, *118*, 7755.

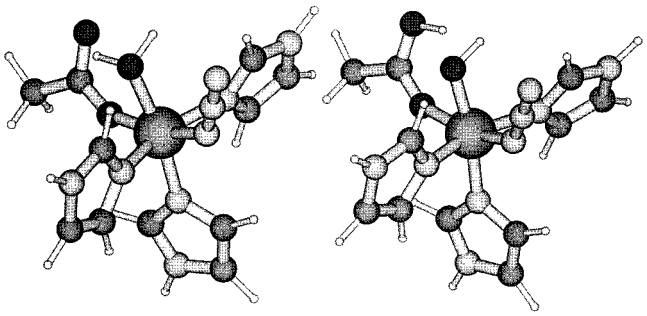

Figure 4. Structures of M^{III}SOD−azide complexes (M = Mn, Fe). In tautomer I, the additional proton resides on the hydroxyl group to form H_2O, while in tautomer II, the proton is transferred to the aspartic acid.

coordinate site can be occupied by substrate O_2^- or inhibitors such as N_3^-, OH^-, OCN^-, and F^-. The binding modes of these inhibitors are expected to resemble those of various intermediates of the catalytic cycle (superoxide, hydroperoxide, and peroxide anions) geometrically and energetically to some extent. Of these, azide (N_3^-) is a good analogue to hydroperoxide (OOH^-), and to $O_2^{-\bullet}$ to a lesser degree, on the basis of charge, size, and geometry. Unlike the short-lived $O_2^{-\bullet}$ adduct, Mn-SOD−azide complex is stable and can be characterized by structural methods. Lah et al. reported the X-ray structures of azide complex of MnSOD from *T. thermophilus* and azide complex of FeSOD from *E. coli*.[14] They found a distorted octahedral geometry at both Mn and Fe sites and, accordingly, proposed a reaction mechanism for superoxide dismutation in which the central metal cations in the active site alternate between five- and six-coordination. Whittaker et al. used optical spectroscopy methods[39,42] to study Mn^{III}SOD−azide complex and found that the geometry of the complex is temperature dependent, exhibiting thermochromism and going from a lower temperature six-coordinate form to a higher temperature five-coordinate form. Also, it is not the azide ligand that is lost but rather, with increasing temperature, either the bound water or the aspartic acid dissociates. Compared to resting Mn^{III}SOD, Mn^{III}SOD−azide has picked up an additional proton, which can reside either on the aspartic acid or on the hydroxyl group forming H_2O. These observations are critical for understanding important aspects of the reaction mechanism.

We carried out geometry optimization on Mn^{III}SOD−azide complex by adding azide to the active site cluster model A, forming $MnL_5-N_3^-$. Two tautomeric forms were optimized, in which the additional proton resides either on the aspartic acid or on the hydroxyl group, as shown in Figure 4. The optimized metal−ligand bond lengths are summarized in Table 4, together with the experimental data for comparison. The same optimization was done for the Fe^{III}SOD−azide complex, and the results are included in Table 4 as well. It can be seen from Table 4 that our optimized metal−ligand bond lengths are in good agreement with experimental data. The largest deviation is in Mn−N(azide) and Fe−N(azide) distances, about 0.2 Å. It is very likely that this difference is largely due to azide−Tyr(36, 34) electrostatic and hydrogen bonding, which is not yet included in the active site quantum model. For MnSOD−azide complex, tautomer II compares better with experimental values, especially for the Mn−O(Asp166) distance. This bond stretches dramatically due to azide binding, from 1.77 to 2.25 Å as observed experimentally.[14] Our calculation for tautomer II reproduces this trend. (From Tables 3 and 4, Mn−O(Asp166) changes from 1.92 to 2.20 Å for tautomer II, model A.) On the basis of these calculations, we suggest that the additional proton associated with azide binding resides on the aspartic acid, resulting in a weakening of the Mn−O(Asp166) bond. As shown in schemes III and IV, this weakening of the Mn−O(Asp166) bond is easily understood in terms of classical valence bond pictures. In III, the Mn−(Asp) bond is a single covalent bond,

Table 4. Metal−Ligand Bond Lengths (Å) of Mn^{III}SOD−and Fe^{III}SOD−Azide Complexes

	optimization				optimization		
	I[c]	II[d]	exptl[a]		I	II	exptl[b]
Mn−O(Wat)	2.062	1.876	1.95	Fe−O(Wat)	1.986	1.984	2.00
Mn−N(170)	2.122	2.093	2.12	Fe−N(160)	2.154	2.168	2.15
Mn−N(28)	2.095	2.005	2.12	Fe−N(26)	2.139	2.137	2.21
Mn−N(83)	2.145	2.064	2.07	Fe−N(73)	2.155	2.127	2.13
Mn−O(166)	1.988	2.196	2.25	Fe−O(156)	2.086	2.092	2.03
M−N(azide)	1.934	1.998	2.22	Fe−N(azide)	1.913	1.904	2.12

[a] From *T. thermophilus* MnSOD, ref 14. [b] From *E. coli* FeSOD, ref 14. [c] Tautomer I. [d] Tautomer II.

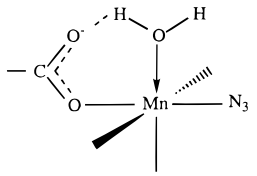

III

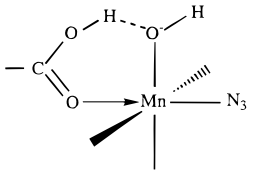

IV

while in IV, it is a dative bond. The latter is weaker and longer, similar to the situations in Mn−OH^- and Mn−OH_2 bonds. For Mn^{III}SOD−azide complex, tautomer II is about 4 kcal/mol more stable than tautomer I.

The geometrical and energetic difference between the two tautomers of Fe^{III}SOD−azide complex is smaller. Rather, the two tautomers tend to converge to nearly the same geometry where the additional proton is between the aspartic acid and the hydroxyl group via a strong hydrogen bond. Experimentally, only a relatively small Fe−O(Asp156) stretch, about 0.18 Å, was observed.[14] This is in accord with our calculations which show that, with azide binding, there is no obvious proton transfer to, or protonation of, the aspartic acid. Such a difference between Mn- and FeSOD−azide complexes may be relevant to some differences in their mechanisms of superoxide dismutation.

3. Redox Potentials and Absolute pK_a Values. According to eq 1, we calculated the redox potentials of the active site clusters both in protein/solvent and in purely solvent environments. The ΔE_{redox} values, together with IP_{red} and ΔE_{pr}, are presented in Table 5. As discussed in our previous paper,[17a] we did not taken into account the intraprotein interaction energy in the calculation of protein field energy E_p, and therefore, we used the same protein structure for both the reduced and oxidized forms. We docked both the reduced and oxidized clusters back to the reduced protein, carried out the calculations in this protein, and obtained the redox potential of the active site cluster in the reduced protein. Similar calculations were done using the oxidized protein. As can be seen from Table 5, the difference between the two sets of values obtained using the reduced and oxidized protein structures is small. For comparison, we also computed the reaction field energy E_r for putting the active site clusters in pure solvents with dielectric constants $\epsilon = 4$ and 80, which correspond to a protein-like low dielectric solvent and

(42) (a) Whittaker, J. W.; Whittaker, M. M. *Biochemistry* **1996**, *35*, 6762. (b) Whittaker, J. W. *J. Phys. Chem. B* **1996**, *101*, 674. (c) Whittaker, J. W.; Whittaker, M. M. *J. Biol. Inorg. Chem.* **1997**, *2*, 667.

Table 5. Calculated Redox Potentials[a]

cluster model	IP_{red}	reduced protein ΔE_{pr}	reduced protein ΔE_{redox}	oxidized protein ΔE_{pr}	oxidized protein ΔE_{redox}	solvent ($\epsilon = 4$) ΔE_r	solvent ($\epsilon = 4$) ΔE_{redox}	solvent ($\epsilon = 80$) ΔE_r	solvent ($\epsilon = 80$) ΔE_{redox}
H_2O form									
A(full)	8.97	−3.99	0.55	−4.05	0.49	−3.34	1.20	−4.37	0.18
A	9.27	−3.85	0.99	−4.07	0.76	−3.35	1.48	−4.38	0.45
B	5.89	−0.01	1.45	−0.07	1.39	−0.39	1.07	−0.43	1.04
C	5.59	−0.31	0.85	−0.33	0.83	−0.32	0.84	−0.30	0.87
D	6.34	−0.44	1.47	−0.48	1.43	−0.46	1.45	−0.50	1.41
OH^- form									
A(full)	4.33	−0.85	−0.95	−0.98	−1.08	−0.77	−0.87	−0.94	−1.03
A	3.92	−0.58	−1.09	−0.67	−1.18	−0.57	−1.08	−0.64	−1.15
B	1.63	1.81	−0.99	1.71	−1.09	1.35	−1.45	1.83	−0.97
C	1.57	1.30	−1.56	1.18	−1.67	1.22	−1.64	1.68	−1.18
D	1.81	1.37	−1.25	1.30	−1.32	1.18	−1.44	1.66	−0.96

[a] IP_{red} and ΔE_{pr} in eV, ΔE_{redox} in V.

Table 6. Calculated Absolute pK_a Values[a]

cluster model	PA	reduced protein ΔE_{pr}	reduced protein pK_a	oxidized protein ΔE_{pr}	oxidized protein pK_a	solvent ($\epsilon = 4$) ΔE_r	solvent ($\epsilon = 4$) pK_a	solvent ($\epsilon = 80$) ΔE_r	solvent ($\epsilon = 80$) pK_a
Mn(II) form									
A(full)	277.7	15.9	18.9	18.4	20.7	17.0	19.7	20.7	22.4
A	285.8	10.7	21.1	10.1	20.6	12.4	22.3	13.8	23.3
B	337.9	−38.8	22.9	−36.6	24.6	−28.5	30.5	−38.8	22.9
C	337.1	−26.0	31.7	−23.7	33.4	−24.1	33.1	−32.7	26.8
D	333.0	−25.2	29.3	−24.0	30.1	−22.1	31.5	−30.5	25.4
Mn(III) form									
A(full)	170.6	88.2	−6.5	89.0	−5.9	76.3	−15.2	99.9	2.0
A	162.5	86.2	−13.9	88.6	−12.1	76.6	−20.9	100.1	−3.7
B	239.6	3.2	−18.2	4.5	−17.2	11.7	−12.0	5.3	−16.6
C	244.4	11.0	−9.0	11.4	−8.7	11.3	−8.8	12.9	−7.6
D	228.5	16.5	−16.6	17.1	−16.4	15.8	−17.1	19.4	−14.5

[a] PA, ΔE_{pr}, and ΔE_r in kcal/mol, pK_a in pH units.

an aqueous solution, respectively. The calculated ΔE_{redox} values have different signs for the H_2O and OH^- forms in all of the cluster models and both for protein and for purely solvent environments. The positive sign for the H_2O form indicates that Mn(II)−H_2O is more stable than the Mn(III)−H_2O form (relative to a standard hydrogen electrode), while the negative sign for the OH^- form reveals that Mn(III)−OH is the more stable. With increasing size of the cluster models, the calculated ΔE_{redox} values vary over a rather large range.

Calculation of absolute pK_a values was done according to eq 2, and the results are shown in Table 6. The calculated pK_a values are positive for Mn(II) forms while they are negative for Mn(III) forms, which indicates a strong basicity for Mn(II) clusters and a strong acidity for Mn(III) clusters. No experimental pK_a values of ligated water in MnSOD are available; the only known relevant data are the pK_a values for naked Mn^{2+} (10.7) and Mn^{3+} (0.1) in aqueous solution.[43] Compared to these values, our calculated pK_a values are larger in absolute value with very negative (acidic) pK_a values for $Mn^{III}(H_2O)$ and very positive values for $Mn^{II}(H_2O)$. A rationale is that the nearby protein ligands and their geometry with respect to the cluster modulate the acidity and basicity of the Mn ions to a rather large extent.

A more detailed argument along these lines can be formulated to explain why the acidity for $Mn^{III}H_2O$ and the basicity of $Mn^{II}OH^-$ are probably overestimated. The strong acidity expected for $Mn^{III}H_2O$ indicates that, under typical pH conditions, only the $Mn^{III}OH^-$ state is likely to be significantly populated. For the reduced Mn(II) state, only the $Mn^{II}H_2O$ is likely to be significantly populated. The available protein X-ray structures will then reflect energetic and geometric adaptations to the oxidation and protonation states that are dominant. Because of this, use of the available protein X-ray structures will give an energetic bias against the $Mn^{III}H_2O$ and $Mn^{II}OH^-$ states that are negligibly populated. Further, these states have different total active site charges from one another and from the dominant $Mn^{III}OH^-$ and $Mn^{II}H_2O$ states (note that the dominant states have the same total charges since $Mn^{III}OH^- + e^- + H^+ \rightarrow Mn^{II}H_2O$ for all cluster models). A further consequence of this argument is that the coupled redox potentials (Table 7) should be calculated more accurately than either redox potential in a fixed protonation state (Table 5) or absolute pK_a's (Table 6). In fact, only the energies of $Mn^{III}OH^-$ and $Mn^{II}H_2O$ are truly needed for the coupled redox calculation; the relative energies of the very unstable intermediates $Mn^{II}OH^-$ and $Mn^{III}H_2O$ with respect to $Mn^{III}OH^-$ and $Mn^{II}H_2O$ are convenient (see eq 4) but not really necessary. In addition, it is chemically reasonable that the $Mn^{III}OH^-$ complex will protonate at the Asp166, and that the five-coordinate $Mn^{II}H_2O$ complex will, at basic pH, hydrolyze an H_2O bound at the sixth coordination site, leaving OH^- bound. Both of these processes should yield more reasonable pK_a's, but we have not evaluated these processes yet.

Table 7. Coupled Redox Potentials (V)

cluster model	protein reduced	protein oxidized	protein av	solvent $\epsilon = 4$	solvent $\epsilon = 80$
A(full)	−0.24	−0.26	−0.25	−0.11	−0.12
A	−0.25	−0.37	−0.31	−0.17	−0.18
B	−0.05	−0.04	−0.05	−0.05	−0.02
C	−0.09	−0.10	−0.10	−0.09	0.00
D	+0.07	+0.05	+0.06	+0.02	+0.13
A (Fisher et al.)[c]					−1.09
exptl	0.26[a]				
	0.31[b]				

[a] For *B. stearothermophilus* enzyme, ref 44. [b] For *E. coli* enzyme, ref 44. [c] Reference 16a.

In any event, from the calculated redox potentials in Table 5 and the pK_a values in Table 6, we can estimate the coupled redox potentials according to eq 4. The calculated results are shown in Table 7. This coupled redox potential corresponds to process 3 and therefore can be compared directly with the experimental redox potential measurements for these enzymes. Two sets of experimental redox potentials for MnSOD have been reported for *E. coli* and *B. stearothermophilus* MnSOD,[44] and they are included in Table 7 as well. The calculated redox potentials in proteins range from −0.31 to +0.06 V. In the largest model, model D, the calculated values are +0.07 and +0.05 V in reduced and oxidized proteins, respectively, which compare fairly well to the experimental values of 0.26 (*B. stearothermophilus*) and 0.31 V (*E. coli*).[44] In the fourth column of Table 7, we list the coupled redox potential values averaged over the reduced and oxidized proteins. Figure 5 depicts the calculated coupled redox potentials for four cluster models. Figure 5 clearly demonstrates the convergence of calculated coupled redox potentials with the increase of the cluster size. Figure 5 also shows that the geometry optimization improved the calculation results significantly. Without optimizing the

(43) (a)Yatsimirksii, K. B.; Vasil'ev, V. P. *Instability Constants of Complex Compounds;* Pergamon: Elmsford, NY, 1960. (b) Cotton, F. A.; Wilkinson, G. *Advanced Inorganic Chemistry*, 5th ed.; John Wiley and Sons: New York, 1988.

(44) Lawrence, G. D.; Sawyer, D. T. *Biochemistry* **1979**, *18*, 3045.

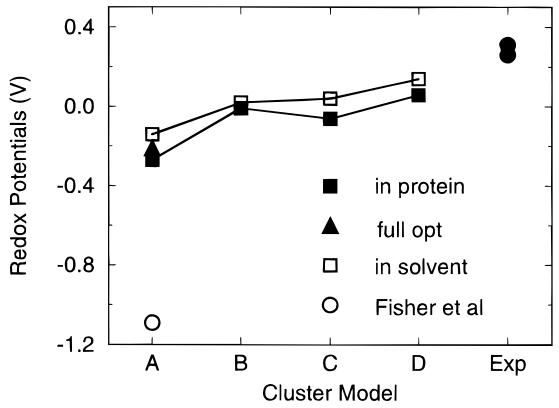

Figure 5. Convergence of calculated coupled redox potentials with different cluster models.

cluster structures for oxidized and reduced states (taking only the single experimental geometry from "oxidized" human MnSOD), the calculated value was far away from the experimental value as we found in previous work (see Fisher et al.,[15] also as shown in Table 7 and Figure 5). Altogether, the geometry optimization of the active site cluster, the enlargement of the cluster model, and the inclusion of the protein environment improve the calculated coupled redox potential over previous results by about 1 V.

It is interesting that the calculated coupled redox potential values are relatively insensitive to environments. By changing the dielectric constant in a purely solvent environment from $\epsilon = 4$ to $\epsilon = 80$, the change in calculated coupled ΔE_{redox} is rather small, especially for the smaller cluster models. This is understandable since the process (3) corresponding to these ΔE_{redox} values is a redox coupled proton transfer procedure, and the overall charge change during this procedure is 0. In particular, the larger clusters in models B, C, and D are not highly charged, there being a net charge of +1 for both the $Mn^{III}OH^-$ and $Mn^{II}H_2O$ forms for model A and 0 for models B−D. As a result, the difference in the overall electrostatic contribution during the coupled redox−protonation process is relatively small, but not negligible. From Tables 5 and 6, the effect of ΔE_{pr} on the coupled redox potential varies from −0.17 V in model A to +0.27 V in model D.

There are several factors which were not taken into account in the reported calculations. As the intraprotein energy term was omitted, the energy change associated with protein geometry changes upon reduction was ignored. Although we have the reduced and oxidized protein structure data, we can only calculate the cluster−protein interaction energy of both reduced and oxidized clusters in reduced or oxidized protein, respectively, and take the average of the values of the proteins in two oxidation states, as shown in the fourth column in Table 7. In this sense, we have considered the protein relaxation effect upon reduction to the final results in a very rough way. We also ignored the polarization of the clusters induced by the protein and solvent reaction fields as we only adopted the one-step, non-self-consistent MEAD method to estimate cluster−protein and cluster−solvent interaction energies. The entropy contribution associated with the coupled reduction and protonation was omitted as well. All these factors can contribute to the error in the calculations along with intrinsic errors in the current density functional methods used.

4. Second Ligand Shell in Active Site Clusters and the Protein/Solvent Reaction Fields. From the viewpoint of coordination chemistry, the active site cluster model, A, which includes the first-shell ligands, is good enough to mimic the main ligand field and coordination environment surrounding the Mn cation. However, it can be seen from Table 7 and Figure 5 that the enlargement of the cluster model, especially the inclusion of the second-shell ligands, Glu169B (represented by an acetate) and Gln151 (represented by a formamide), plays an important role in improving the energy calculations. From model A to model B, the calculated coupled redox potential ΔE_{redox} shifts up by about 0.26 V, and from model B to model D, the calculated ΔE_{redox} shifts up another 0.11 V.

The Glu169B is not directly coordinated to the Mn atom, and the Mn−OE distances are about 7.0 Å in the oxidized protein. Instead, it connects to the imidazole ring of His170 in the active site cluster via an OE2···H···ND1 hydrogen bond. As a second-shell ligand, the Glu169B is not as important in modulating the ligand field of the central metal cation; however, it is vital in stabilizing the whole active site cluster via the electrostatic interaction and hydrogen bonding with the histidine. In Figure 6, we depict the decomposition of individual residue contributions to the protein field energy E_p for the smallest cluster model, A. Figure 6 clearly shows that the electrostatic interaction between residue Glu169B and the active site cluster is the largest contribution to E_p, about −7.6 kcal/mol. However, the electrostatic interaction with the active site cluster is not the only role played by Glu169B, as we will show from quantum calculations on the larger clusters discussed below. While electrostatically significant for both the oxidized and reduced clusters (model A), the contributions of residue Glu169B to E_p's of $Mn^{III}(OH^-)$ and $Mn^{II}(H_2O)$ clusters largely cancel each other and make no significant contribution to ΔE_{pr} and ΔE_{redox}; see Figure 6C. It is therefore very natural to switch this residue from the "classic" electrostatic region into the quantum cluster, in which the OE2···H···ND1 hydrogen bond (and particularly charge transfer) is described more properly by quantum calculations. This hydrogen bond is enhanced by a charge transfer from the negatively charged OE2 atom to the positively charged cluster, and, in the gas phase calculations using cluster model B, the hydrogen-bond strength amounts to −73 kcal/mol in the $Mn^{II}(H_2O)$ form and −74 kcal/mol in the $Mn^{III}(OH^-)$ form. Certainly, this charged hydrogen bonding interaction is very strong. It reflects not only the Glu169B interactions with the His170 ND proton but also strong electrostatic attraction of the carboxylate (COO^-) to His170 and other nearby positively charged groups in the quantum cluster (Mn(II), Mn(III), and His28, His83, see Figure 2). We have explored the large difference between the gas phase hydrogen-bond strength (−73 kcal/mol) and the much smaller Glu169B protein field−cluster interaction energy (−7.6 kcal/mol). This discrepancy arises largely because the protein field is screened by the protein and solvent dielectrics ($\epsilon_p = 4$, $\epsilon_s = 80$), while there is no such screening of the Glu169B−$[MnL_4(H_2O)]$ gas phase interaction. Using the same Glu169B−cluster electrostatic interaction, but with no screening ($\epsilon_p = 1$, $\epsilon_s = 1$), gives an energy of −67.8 kcal/mol, comparable to the fully quantum model. The "effective" dielectric constant for the screened Glu−cluster interaction is then $\epsilon_{eff} = 8.9$, which arises from both the protein dielectric and the solvent funnel near the active site. We will argue that, for these strong interactions, it is better to go to the larger quantum clusters (models B, C, and D rather than A). Such strong/short charge−charge interactions are not effectively screened by nearby protein dipoles (as is assumed when $\epsilon_p = 4$ is used). However, at least some of the solvent screening (by the solvent funnel) of the Glu169B protein field interaction term in model A will instead contribute to the reaction field energy term in model B.

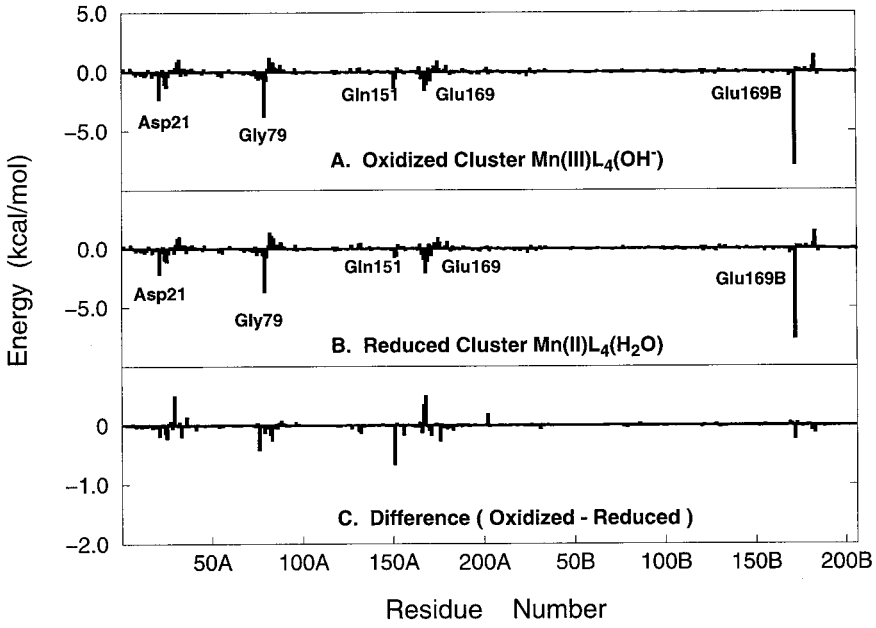

Figure 6. Decomposition of active site cluster (model A) protein interaction energy E_p to individual residues in *T. thermophilus* MnSOD enzyme: (A) oxidized cluster $Mn^{III}L_4(OH^-)$ in oxidized enzyme; (B) reduced cluster $Mn^{II}L_4(H_2O)$ in reduced enzyme; (C) difference (oxidized − reduced).

Table 8. ESP Charges of Active Site Cluster Models A−D in $Mn^{III}(OH^-)$ (Ox) and $Mn^{II}(H_2O)$ (Red) Forms

	A		B		C		D	
	Ox	Red	Ox	Red	Ox	Red	Ox	Red
Mn	1.038	0.921	1.035	0.935	1.043	0.796	1.042	0.763
Wat205	−0.275	0.040	−0.289	0.042	−0.278	0.072	−0.255	0.079
His28	0.381	0.316	0.321	0.274	0.298	0.379	0.321	0.388
His83	0.190	0.165	0.141	0.113	0.147	0.102	0.155	0.149
Asp166	−0.532	−0.596	−0.585	−0.625	−0.580	−0.532	−0.561	−0.503
His170	0.199	0.154	0.146	0.091	0.040	0.035	0.011	0.046
Glu169B			−0.771	−0.828	−0.750	−0.785	−0.745	−0.790
NH168					−0.054	−0.052	−0.057	−0.055
NH170					0.135	−0.015	0.136	−0.010
Gln151							−0.050	−0.070
total	1.0	1.0	0.0	0.0	0.0	0.0	0.0	0.0

Table 8 shows the ESP charges of various groups in the MnSOD active site models. The data in Table 8 indicate that, in the reduced $Mn^{II}(H_2O)$ form of the clusters, about 0.2 electron is transferred from the acetate group of Glu169B to the Mn center and its first-shell ligands. In the oxidized $Mn^{III}(OH^-)$ form, the electron transfer increases to some extent. It is only by including such electron transfer effects and the hydrogen bond between the second and first ligand shells in a proper way that the calculated ΔE_{redox} can be improved significantly.

An examination of the IP_{red} and ΔE_{pr} values for cluster models A and B in Table 5 is instructive for a further understanding of the role of the second-shell ligand, Glu169B. If we focus on the changes of IP_{red} and ΔE_{pr} with the enlargement of the quantum cluster size, it is found that the most significant changes occur when Glu169B is added (model A to B). The addition of an acetate $CH_3CO_2^-$ group to model A ($MnL_4(H_2O)$ form) decreases the IP_{red} by about 3.4 eV. As compensation, ΔE_{pr} shifts up by about 3.8 eV. These data once again show that Glu169B contributes the largest part of the protein−active site cluster interaction and that it buffers the electrostatic impact caused by adding an electron to the active site center. It can also be seen from Table 7 that the inclusion of two simple amine molecules in the quantum model (model B to model C), which represent the hydrogen bonds between His170 backbone to Glu169B side chain and Trp168 main chain to Asp166 side chain, has only a moderate effect on the energetics. The apparently modest energetic role of the Trp168 (N−H) hydrogen bond to O(Asp166) is rather deceptive, as discussed previously. This hydrogen bond orients the Asp166 carboxylate side chain and weakens the O(Asp)···H···OH hydrogen bond (Figure 3). This accounts for the main energetic difference between the coupled redox potentials of model A(full) vs model A(constrained).

Gln151 is another important second-shell ligand. The NE2 atom of this ligand is about 4.6 Å away from the central Mn cation. It forms a hydrogen bond to the ligated water or OH^- group and is involved in the proton relay system consisting of Wat205, Gln151, Trp169, and Tyr36. A mutagenesis study of this amino acid in human mitochondrial MnSOD (Gln143 → Asn) revealed that the Gln → Asn mutation modulates the reduction potential, which indicates that this Gln is important in the redox process.[12] As can be seen from Figure 6 and Table 8, although the electrostatic interaction between this residue and the active site cluster is not very strong and the charge transfer from Gln151 to the Mn center and the ligated H_2O/OH^- group is not dominant, switching the side chain of Gln151 from the pure electrostatic region to the active site quantum cluster shifts the calculated redox potential up and closer to experiment by 0.16 V (Table 7). In the largest cluster model D, the hydrogen bond, O···H···NE2, is now described properly by quantum calculations, and the strength of this hydrogen bond is about −6 kcal/mol for the $Mn^{II}(H_2O)$ form and −7 kcal/mol for the $Mn^{III}(OH^-)$ form in the gas phase. For both Glu169B and Gln151, the total redox shift (model A to B, C to D) involves a number of terms. For example, the gas phase hydrogen-bond-strength difference contributes only modestly to the coupled redox potential change.

In Table 9 we present the decomposition of E_{pr} to protein (E_p) and reaction (E_r) contributions for the $Mn^{II}(H_2O)$ and $Mn^{III}(OH^-)$ forms for various cluster models, together with the E_r values in pure solvents. Compared to the reaction field contribution (E_r), the protein component (E_p) is relatively small and only contributes about 10−20% of the total E_{pr}. This indicates a strong electrostatic interaction between the active

Table 9. Protein Field (E_p) and Reaction Field (E_r) Contributions to E_{pr}

	in oxidized protein			in reduced protein			in solvent E_r	
	E_r	E_p	E_{pr}	E_r	E_p	E_{pr}	$\epsilon = 4$	$\epsilon = 80$
Reduced Cluster, H_2O Form								
A	−51.5	−10.1	−61.6	−54.8	−8.7	−63.5	−46.1	−64.0
B	−53.4	−15.2	−68.6	−54.4	−13.4	−67.8	−43.7	−63.1
C	−48.5	−5.1	−53.6	−48.4	−5.0	−53.4	−39.6	−58.2
D	−52.8	−7.0	−59.7	−53.1	−6.2	−59.3	−43.6	−64.4
Oxidized Cluster, OH^- Form								
A	−55.8	−11.2	−67.0	−55.8	−10.3	−66.1	−46.8	−65.0
B	−51.6	−14.3	−65.8	−51.5	−13.4	−64.9	−41.1	−59.7
C	−44.5	−5.4	−49.9	−44.4	−5.0	−49.4	−35.7	−52.1
D	−47.4	−6.4	−53.8	−47.4	−5.6	−53.0	−38.5	−56.6

site cluster and protein−solvent dielectrics. From these data, it can be concluded, as in our previous paper,[17a] that the reaction field provides a "coarse tuning" of the redox potential while the protein field provides a "fine-tuning". In general, with increasing size of the active site quantum clusters, the absolute values of protein contributions, E_p, decrease because parts of the electrostatic interaction have been included in the quantum clusters. Moreover, the relative trend of E_{pr} for $Mn^{II}(H_2O)$ and $Mn^{III}(OH^-)$ has been inverted by increasing size of the cluster models from A to D. In model A, the E_{pr} for the reduced $Mn^{II}(H_2O)$ form is less negative than that for the oxidized $Mn^{III}(OH^-)$ form, while in models B−D, E_{pr} for the $Mn^{II}(H_2O)$ form is more negative than that for the $Mn^{III}(OH^-)$ form. As a result, the reduced $Mn^{II}(H_2O)$ form is more stabilized and the calculated ΔE_{redox} is shifted up closer to the experimental values. In going from the cluster model A to model D, ΔE_{redox} changes by 0.37 V, of which 0.44 V is the ΔE_{pr} term while the gas phase intracluster quantum energy difference contributes the remainder (of opposite sign).

V. Conclusions

We have demonstrated in this paper that the redox potential of the enzyme MnSOD can be calculated by combined density functional theory and electrostatic methods. The active site cluster and the protein/solvent environment of MnSOD in *T. thermophilus* were treated by density functional theory in a protein and solvent environment. The calculated coupled redox potential, which corresponds to a redox procedure coupled with protonation or proton transfer, was +0.06 V for *T. thermophilus* MnSOD, which compares well with the experimental measurements of +0.26 V for *B. stearothermophilus* and +0.31 V for *E. coli* enzymes.[44] This result represents a significant improvement over our previous redox calculation of the MnSOD active site in solution. The improvement was achieved by three means: (1) the geometry optimization of the active site cluster, (2) the enlargement of the cluster model to contain some second-shell ligands, and (3) the inclusion of the protein/solvent environment.

Although the geometries of enzyme active sites can be determined by protein X-ray crystallography, the geometric data obtained in this way, even at good resolution, may possess significant uncertainties and may not be accurate enough for energetic calculations. Our optimized geometries of the MnSOD active site are in good agreement with the X-ray crystallographic data for the reduced form, with an average error in Mn−ligand bond length less than 0.1 Å. However, for the oxidized active site, the optimized Mn−ligand distances are shorter than indicated by X-ray data, especially for Mn−O(Wat) distances. However, the experimental bond lengths are very close to the "mixed" calculated bond lengths which are an average of corresponding bond lengths in reduced and oxidized active sites. It can be concluded from these results that the experimental X-ray data for the oxidized active site, especially that for human mitochondrial MnSOD[7] and *T. thermophilus* MnSOD,[10] probably do not correspond to a pure oxidized enzyme. Instead, these data may correspond to a physical mixture of oxidized and reduced enzymes due to the redox heterogeneity, in agreement with EPR experiments.[39] The optimized geometries provide a good starting point for accurate energetic calculations.

The second-shell ligands, although not directly bonded to the central metal cations, are indispensable for accurate energetic calculations. Augmentation of the active site cluster by side chain ligands from Glu169B and Gln151 shifted up the calculated coupled redox potentials by about +0.4 V, bringing them closer to the experimental values. Glu169B is strongly bound to a first-shell histidine ligand via a charged hydrogen bond, and Gln151 lies in the center of the proton relay system. The incorporation of these second-shell ligands into the active site quantum cluster improves the description of the hydrogen-bond network, long-range electrostatic interactions, and charge transfer effects.

Acknowledgment. This work was supported by NIH Grants GM50154 to L.N. and GM45607 to D.B. We thank E. Stroupe for discussions and ongoing comparative work on related systems. We thank Dr. V. Dillet for her work on the protein energy decomposition analysis. We are very grateful to Drs. D. A. Case, J. A. Tainer, D. E. McRee, and M. L. Ludwig for many useful discussions and E. J. Baerends and the Amsterdam group for use of the ADF package. The calculations were carried out on the SGI Power Challenge and Cray T3E computers at The Scripps Research Institute.

IC980731O